ETH
Eidgenössische Technische Hochschule Zürich
Swiss Federal Institute of Technology Zurich

ARSL
Acoustic Robotics Systems Lab

Lilian Laporte

Real-Time Ultrasound Imaging Feedback

Semester Thesis

Acoustic Robotics Systems Lab
Swiss Federal Institute of Technology (ETH) Zurich

Professor

Prof. Dr. Daniel Ahmed

Supervision

Mahmoud Medany

January 2024

Contents

Acknowledgments

This semester thesis was written at ETH Zurich as part of the Acoustic Robotics Systems Laboratory (ARSL) in collaboration with the Binning and Rohrer Nanotechnology Center (BRNC).

Firstly, I would like to thank my supervisor, Mahmoud Medany, for his time and valuable inputs throughout the thesis. Additionally, I would like to thank all members at ARSL for lending a helping hand whenever necessary.

Finally, I would like to express my gratitude to Prof. Dr. Daniel Ahmed and the administrative staff of the ARSL for their unwavering support throughout the completion of this thesis.

Abstract

Since the latter half of the 20^{th} century, extensive research has underscored the versatility of microbubbles as a contrast agent for Ultrasound (US) imaging. Moreover, their efficacy as a potential drug delivery system (DDS) for treating cancers and central nervous system diseases has been well-documented over the years. In this context, the Acoustic Robotics Systems Lab has embarked on a mission to enhance control over swarms of microbubbles (MB) using transducers, aiming to target specific areas. This thesis introduces a novel approach for achieving real-time feedback through the integration of an US Imaging Machine. By leveraging a HDMI to USB converter, a maximum frame rate of 10 frames per second (fps) and a minimal latency of 0.1 seconds have been attained. Additionally, a comprehensive channel setup utilizing AgarAgar has been implemented to optimize image clarity. However, to address the challenge of poor image quality, a robust tracking algorithm based on DeepSORT has been developed with promising performances. Lastly, a methodology for influencing MB flow under dynamic conditions has been devised with a High Intensity Focused Ultrasound (HIFU).

Acronyms and Abbreviations

ARSL	Acoustic Robotics System Lab
BRNC	Binning and Rohrer Nanotechnology Center
DDS	Drug Delivery System
DeepSORT	Simple Online and Realtime Tracking with a Deep Association Metric
DoF	Degree-of-Freedom
ETH	Eidgenössische Technische Hochschule
FP	False Positive
fps	frame per second
HIFO	High Intensity Focused Ultrasound
IDF1	Identification F1
IoU	Intersection over Union
MB	Microbubble
MOT	Multi Object Tracker
μCT	Micro Computed Tomography scan
MOTA	Multiple Object Tracking Accuracy
NMS	Non-Maximum Suppression
PDMS	Polydimethylsiloxane
ROI	Region Of Interest
TMMP	Tissue Mimicking Phantom
ULM	ultrasound localization microscopy
US	Ultrasound
US-APA	ultrasound Acoustic Phase Analysis
US-OF	ultrasound Optical Flow US-OF

Chapter 1

Introduction

1.1 Ultrasound Imaging

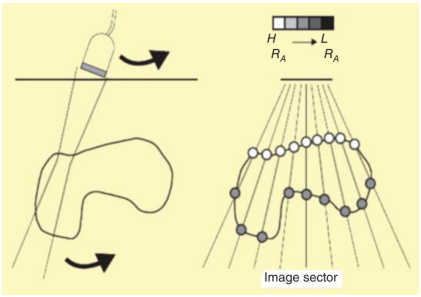

Figure 1.1: Illustration of B-mode imaging system from Ozcelik et al. [1]

Ultrasound imaging, with a history dating back over 40 years, has emerged as a vital diagnostic tool in medicine. Originating from pioneering work in the mid-20th century, ultrasound technology has undergone rapid advancements, from early A-mode and B-mode scanning techniques to modern high-resolution grayscale imaging and real-time Doppler capabilities [2]. Today, ultrasound imaging finds extensive use across medical specialties, offering non-invasive visualization of internal structures and dynamic physiological processes such as blood flow. Sonographers, equipped with a thorough understanding of ultrasound physics and instrumentation, utilize this technology to acquire and interpret images crucial for patient diagnosis and management.

Despite its historical and technological advancements, ultrasound imaging has inherent limitations, such as its inability to penetrate air-filled structures like the lungs or to visualize through bone. Nonetheless, its versatility and accessibility make it indispensable in various clinical scenarios, including obstetrics, gynecology, cardiology, radiology, and emergency medicine [3]. With ongoing advancements in transducer design, signal processing, and imaging algorithms, ultrasound imaging continues to evolve, promising even greater diagnostic capabilities and expanding its role in modern medical practice.

1.1.1 Doppler mode

Doppler mode in ultrasound imaging utilizes the Doppler effect to visualize and measure blood flow within vessels. As ultrasound waves encounter moving blood cells, their frequency shifts in proportion to the velocity of the blood cells. By analyzing these frequency shifts, Doppler ultrasound provides real-time information on blood flow direction and speed, displayed as color-coded images or spectral waveforms [5]. This enables clinicians to assess blood flow patterns, detect abnormalities, and monitor hemodynamic changes, enhancing diagnostic capabilities in cardiovascular medicine.

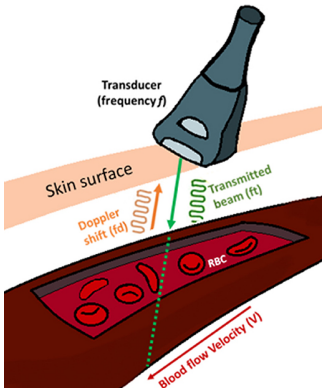

Figure 1.2: Illustration of Doppler mode
from Benslimane et al. [4]

Limitation of Doppler mode

Doppler mode effectively detects MB flow by analyzing frequency shifts of reflected ultrasound waves. However, as shown in Figure 1.3 by the blue rectangle, simultaneous activation of a second transducer can interfere and saturate the Doppler signal, impeding accurate detection of MB flow amidst heightened background noise. This phenomenon occurs regardless of the scale used for the Doppler mode and of the frequency used by the probe. Thus, while Doppler mode remains effective in standard imaging scenarios, its utility may be compromised during concurrent activation of a separate transducer.

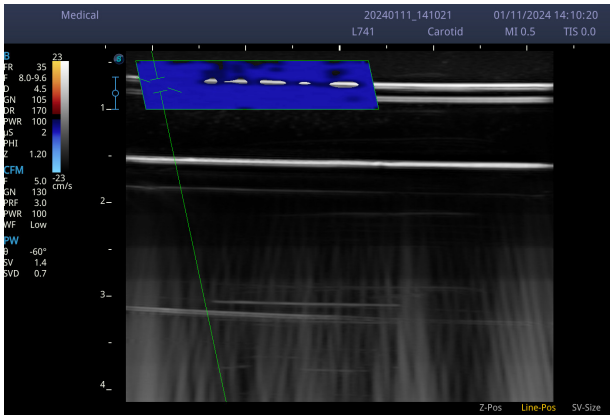

Figure 1.3: Doppler mode while a transducer is activated

1.1.2 Side Effects

Effect on Microbubbles

As Supponen et al. [6] demonstrated, the probe of the US imaging machine has an incontestable effect on the MBs. A simple experiment can demonstrate it. One can let MBs coming in the channels without imaging them. After some time, one can place the probe on the upper part of the gel and move it down until it is as the same level as the channels. The Figure 1.4 illustrates the image of the channels as soon as the probe is at the same level of the channels, and the same image after some time. In less than 1 second, all the MBs vanished. The whole frequency range produces this effect and reducing the intensity of the signal from the probe only attenuates the effect.

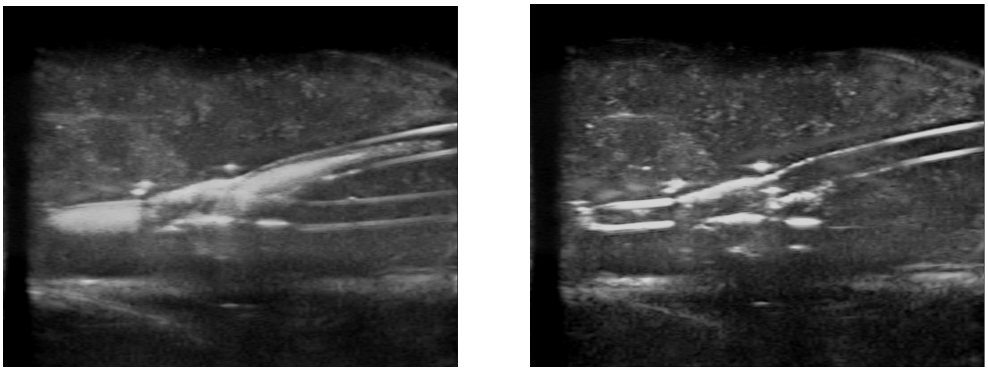

(a) Image of channels at time t (b) Image of channels at time t+0.7s

Figure 1.4: Effect of Ultrasound probe on Microbubbles

Mirror artifacts

Another side effect when using the US probe on the gel used in the setup is the reflection of the acoustic wave on the face on the opposite side from the probe which acts like an acoustic mirror as Kerr and Middleton [7] described it. This is due to the difference of acoustic impedance between the gel matrix and the air. As shown in Figure 1.5, placing an object on the opposite side from the probe in order to not have air anymore, makes the high intensity noise on the lower part of the image disappear.

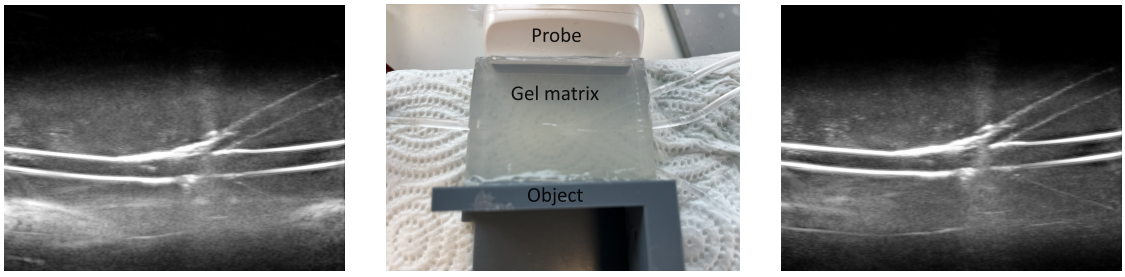

(a) US image without an object on the opposite side (b) Object on the opposite side (c) US image with an object on the opposite side

Figure 1.5: Effect of Gel-Air Interaction on Ultrasound Imaging

1.2 Microbubbles

Bubble reagents, historically pivotal in medical applications, notably serve as contrast agents in ultrasound imaging. In water-filled blood vessels, the presence of bubbles alters acoustic impedance at the gas-liquid interface, generating a reflected echo for US imaging. MBs, distinguished by flexible surfaces, resonate with ultrasound waves, resulting in robust echogenicity. This principle underpins the effectiveness of MBs as contrast agents in ultrasound imaging, enhancing diagnostic precision. Furthermore, the precise control of microbubbles through ultrasound manipulation opens avenues for targeted drug delivery and localized therapeutic interventions, promising advancements in personalized medicine and minimally invasive treatments.

1.2.1 Bubble Reagents as Drug Delivery Systems

MBs, beyond their role as contrast agents in ultrasound imaging, offer a promising avenue for drug delivery in the treatment of various diseases, including cancer [8] and central nervous system diseases [9]. Leveraging their unique properties, MBs can encapsulate therapeutic agents such as chemotherapy drugs or genetic material. These drug-loaded MBs can be targeted to specific sites within the body using ultrasound waves, which can induce MBs oscillations, resulting in localized drug release [10]. In cancer therapy, this targeted drug delivery approach minimizes systemic toxicity and enhances the therapeutic efficacy of anticancer drugs, while in central nervous system diseases, it allows for the delivery of drugs across the blood-brain barrier to reach the affected areas with precision. The use of MBs as a drug delivery service holds considerable potential for revolutionizing therapeutic interventions, offering targeted and minimally invasive treatment options for a range of medical conditions.

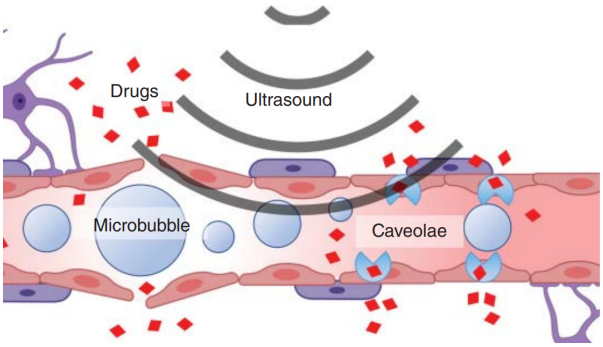

Figure 1.6: Schematic of drug delivery by ultrasound and microbubbles from Ozcelik et al. [1]

1.2.2 Control of Microbubbles

MB control in biomedical applications is facilitated by various strategies, among which the propulsion mechanism plays a pivotal role. As elucidated by Fonseca et al. [11], the propulsion strategy relies on two primary forces: the primary radiation force and the secondary Bjerknes force. These forces enable precise manipulation and navigation of MBs within biological environments, offering opportunities for targeted drug delivery and localized therapy. Additionally, recent advancements in control strategies, such as Reinforcement Learning [12], have emerged to further enhance MB manipulation capabilities. Remarkably, these innovative approaches, exemplified by results showcased in Figure 1.7, demonstrate the potential of advanced control techniques in optimizing MB-based biomedical interventions.

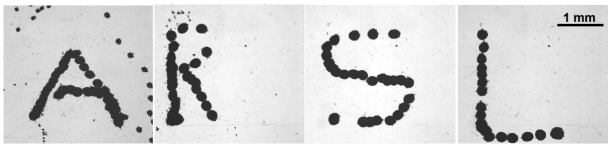

Figure 1.7: ARSL writing using swarm manipulation from Schrage et al. [12]

1.3 Project Overview

This thesis is conducted within ARSL, a laboratory at ETH Zurich established in 2020. ARSL is dedicated to interdisciplinary research in micro/nanorobotics and micro/nanosystems, with a focus on biomedical engineering, diagnostics, and medical applications employing ultrasound technology. The thesis aligns with ARSL's research agenda by contributing to the advancement of in vivo acoustic manipulation systems and the development of multifunctional robotic systems, addressing critical challenges in these areas.

Figure 1.8: ARSL research policy

1.4 Thesis Outline

This thesis is structured as follow: **Chapter 2** provides an overview of related work in the fields of MBs and US imaging followed by the problem statement of the thesis. **Chapter 3** introduces the setup used for the experiments. **Chapter 4** presents an approach in order to detect and track MBs. **Chapter 5** discussed the results of the tracker and of the control ability under US imaging. Finally in **Chapter 6**, the results are summarized, and an outlook on future work is given.

Chapter 2

Related Work

Recent studies have particularly emphasized collective behaviors, enhancing delivery capacity and adaptability, and improving medical imaging contrast. This chapter provides an overview of related work in the field of US image enhancement and of microrobots tracking with US imaging. Finally, it highlights the challenges of the thesis, yielding the problem statement of this thesis.

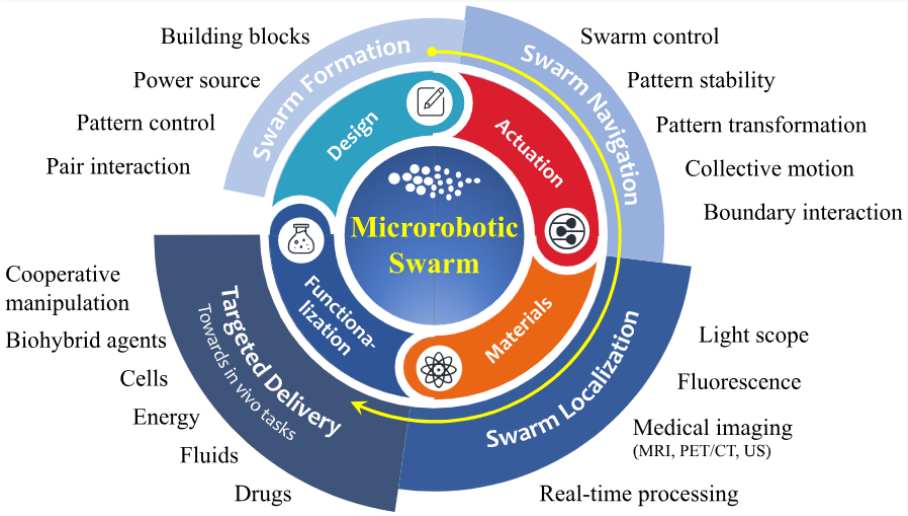

Figure 2.1: Illustration of the key features and steps of using microrobotic swarms for imaging-guided delivery tasks from Wang and Zhang [13]

2.1 Super-resolution with Microbubbles

Currently, ultrasound resolution is constrained by diffraction, restricting it to approximately half the wavelength of the sound wave employed. However, recent advancements in super-resolution imaging techniques have overcome this limitation by precisely localizing and tracking sparse sets of MBs within the vasculature. The following studies present different approaches to this topic.

Andersen et al. (2021) [14] compared the vascular anatomy in two in vivo 2D SRUS images of a Sprague–Dawley rat kidney with ex vivo μCT (Micro Computed Tomography scan) of the same kidney. Co-registering the SRUS images to the μCT volume revealed visually very similar vascular features, indicating a high level of vessel branching complexity captured in the 2D SRUS images. While validating the super-resolution capability of their ultrasound scans proved challenging using μCT data of a whole rat kidney specimen, fundamental challenges for 2D SRUS were highlighted, including the complexity of projecting a 3D vessel network into 2D. These findings underscore the importance of considering such challenges when interpreting clinical or preclinical SRUS data in future studies.

Huang et al. (2020) [15] explored super-resolution ultrasound localization microscopy (ULM), relying on individual MB localization and tracking, to achieve fine microvascular imaging at clinically relevant depths. However, ULM's reliance on dilute MB concentrations leads to long imaging times. To overcome this, they proposed separating overlapping MB events based on spatiotemporal flow dynamics, improving ULM imaging robustness in high-concentration MB injections. Demonstrations in phantom data and chicken embryo models show promise for clinical translation by reducing acquisition times and the need for dilute MB injections.

Hansen et al. (2016) [16] addressed the limitation of ultrasound resolution imposed by diffraction, proposing a technique to achieve super-resolution imaging on non-fixated tissue by compensating for tissue movement and tracking individual microbubbles. Their experiment, conducted on the kidney of an anesthetized Sprague-Dawley rat with SonoVue infusion, demonstrated that motion compensation effectively removed movement caused by mechanical ventilation. Results showed improved microbubble localization precision, reducing the standard deviation of super localizations from 22μm to 8μm. This study suggests the potential elimination of the restriction of using completely fixated tissue for super-resolution imaging with microbubbles.

2.2 Microrobots Tracking with Ultrasound Imaging

The potential of remotely actuated small-scale robots in targeted delivery, micromanipulation, and biosensing has garnered significant attention. Nonetheless, challenges persist in effectively imaging and controlling these robots within expansive workspaces, particularly when navigating through intricate and hard-to-access areas within living organisms. The following studies will offer different strategies to address these challenges.

Du et al. (2022) [17] proposed a strategy for real-time magnetic navigation of an untethered miniature robot using ultrasound image feedback. A mobile

electromagnetic coil-based system was designed to control and simultaneously track the robot in a large workspace. An ultrasound probe integrated with a three degree-of-freedom (DoF) manipulator swept the workspace and actively followed the robot, employing a dynamic region of interest (ROI) for real-time tracking. Experiments in tissue-mimicking phantoms with branching and tortuous environments were conducted. Results showed selective navigation along different paths and long-distance navigation in tortuous environments. Mean transverse deviations between planned and tracked trajectories were less than the tube radius, validating the feasibility of the strategy for navigating miniature robots inside hard-to-reach regions under medical imaging guidance.

Wang et al. (2022) [18] proposed an optimized actuation strategy to enhance ultrasound imaging contrast for a reconfigurable colloidal microswarm. They observed dynamic ultrasound contrast dependent on the coordination between the magnetic field frequency and ultrasound imaging temporal resolution. Analyzing the optimal driven frequency (f_{op}) for enhanced ultrasound contrast at different depths, they experimentally validated it at imaging depths of 3–7 cm. Pattern transformation of the microswarm further enhanced ultrasound contrast, with experimental results aligning well with analytical findings. Additionally, they successfully localized the microswarm ex vivo at depths of 3.4–6.5 cm, reducing nanoparticle dose requirements. Reversible pattern transformation provided morphological adaptability, enabling navigation and reversible pattern transformation in a narrowed channel. Their optimized strategy offers a potential approach for utilizing microrobotic swarms in real-time localization tasks guided by medical imaging.

Botros et al. (2022) [19] investigated a method for detecting and tracking chain-like magnetic microsphere robots using ultrasound imaging in an in-vitro environment. Their approach utilized deep learning techniques to estimate the real-time position of the microrobot. Experimental results demonstrated high accuracy in detecting and tracking spherical microrobots with approximately 500 μm diameter in dynamic environments. They achieved detection and tracking accuracies of around 95% and 93%, respectively, for one, two, and three-sphere microrobots.

Faoro et al. (2024) [20] compared ultrasound Acoustic Phase Analysis (US-APA) with ultrasound Optical Flow (US-OF) for tracking microrobots in tissue-mimicking phantoms. They fabricated cylindrical magnetic microrobots of various dimensions and actuated them using a permanent magnet to mimic intravascular rolling and in-place vibration. US-OF showed comparable performance to US-APA in localizing vibrating microrobots and slightly better during rolling, with tracking errors below 0.6 body length. Moreover, US-OF exhibited superior temporal performance, achieving an output rate forty times higher than US-APA (about 40 Hz in US-OF and about 1 Hz in US-APA). These findings suggest the potential of Optical Flow for microrobots tracking, especially regarding portability and intelligibility.

2.3 Problem Statement

Sections 2.1 and 2.2 explored distinct avenues of research, focusing on super-resolution US imaging through MB tracking and real-time microrobot tracking via US imaging, respectively. Bridging these studies, the development of a real-time US imaging feedback system for MBs integrates elements from both approaches, as demonstrated by Ackermann and Schmitz [21]. The thesis requirements are the following:

- Designing a channel setup compatible with US imaging
- Controlling the flow rate of MBs
- Setting up real-time US data acquisition on a computer system
- Implementing real-time detection and tracking algorithms for MBs
- Integrating control mechanisms for manipulating MBs using transducers

Chapter 3

Setup

3.1 Channels

3.1.1 Polydimethylsiloxane

Polydimethylsiloxane (PDMS) is my first choice for the making of the channels. Due to its acoustic transparency, its moldability and its compatibility with Transducer Coupling, it makes it as a good candidate for Tissue Mimicking Phantom (TMMP) [22].

Recipe

One of the advantages of PDMS is its ease of fabrication. It is composed by the following steps:

- In a container, mix a ratio of 10 parts silicone to 1 part curing agent.
- Stir until the mixture becomes opaque.
- Employ a vacuum machine to eliminate bubbles.
- Pour the liquid into a mold.
- Leave in the oven for 1 hour.
- After curing, carefully remove the border of the molds, leaving only the channel portion embedded in the PDMS.
- Clean the inner part of the channels by immersing them in acetone to remove any residual material.

Choice of the mold

To replicate the body's vasculature and demonstrate control over MBs within, an optimal channel design involves creating a bifurcation. The initial design of the mold is depicted in Figure 3.1.
However, Due to its complexitiy, it is not possible to remove the inner part of the channels with acetone.

Figure 3.1: First design of the mold for PDMS

Hence, a more straightforward design for the bifurcation is suggested. Illustrated in Figure 3.2, rather than incorporating three separate bifurcations merging into a single output channel, a single fork now divides into three distinct outputs. This modification is better suited for use with PDMS, leading to the creation of the fork depicted in Figure 3.3 below.

Figure 3.2: Second design of the mold for PDMS

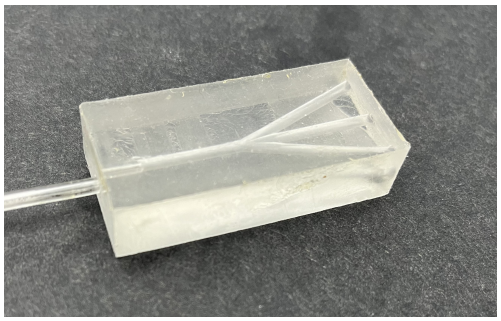

Figure 3.3: Result of the bifurcation made of PDMS

Resulting image

Following initial tests on the first day, I captured an image, as shown in Figure 3.4, using a frequency range of 8 to 9.6 MHz. While the fork's start is evident, the remainder on the right is obscured by the mirror effect detailed in section 1.1.2. However, within a few days, the PDMS became entirely impermeable to US, rendering the channels unobservable. A different solution was therefore necessary.

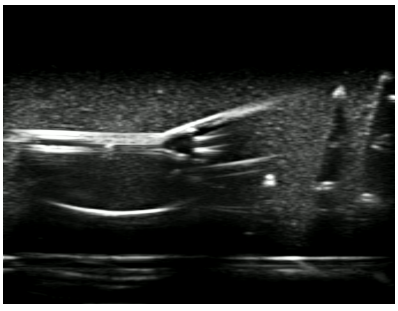

Figure 3.4: Resulting image with the bifurcation made of PDMS

3.1.2 AgarAgar

Another option for TMMP is to utilize Agar Agar powder [23]. Its acoustic properties are noteworthy as it is acoustically transparent, ensuring clear and precise US images. However, the resulting gel matrix is fragile and must be remade daily due to slow water leakage.

Recipe

The fabrication process is straightforward and can be completed quickly. It involves the following steps:

- Prepare the mold by inserting the tubes inside and by plugging the holes with black tape
- Boil 150 mL of water in a pot.
- Add 8g of Agar Agar powder[1] (equivalent to 1 sachet) into the boiling water.
- Reduce the heat intensity and stir the mixture for 3 minutes.
- Pour the liquid Agar Agar solution into a mold.
- Allow the mixture to set by refrigerating it for at least 1 hour.
- Carefully remove the solidified gel from the mold.

Tubes

Since Agar Agar gel is not waterproof, simply adding water will not yield accurate observations. Utilizing tubes becomes necessary to establish channels within the gel. Among the available tubes, the Heat Shrink Tube[2] proves the most suitable option, commonly used for soldering. Its thinness ensures compatibility with US imaging, minimizing acoustic wave scattering. Additionally, its shrink capability facilitates connection with other tubes or itself. Creating a bifurcation with two outputs involves cutting a hole in a tube and attaching another, as shown in Figure 3.5. Likewise, assembling three tubes together produces the same configuration, as seen in Figure 3.6. For a more complex design, a three-output bifurcation made from three tubes is depicted in Figure 3.7.

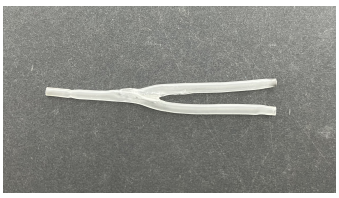

Figure 3.5: 2 outputs fork made of 2 tubes

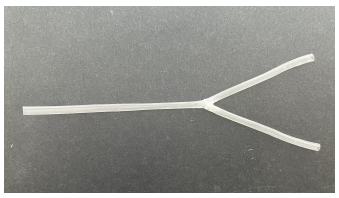

Figure 3.6: 2 outputs fork made of 3 tubes

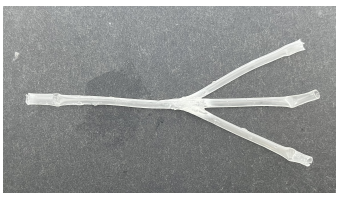

Figure 3.7: 3 outputs fork made of 3 tubes

[1]The Agar Agar powder used is from the brand Pâtissirer

[2]The tubes used are from TRU Components and have a diameter of 2mm. the shrink ratio is 2:1 and the color is clear.

Choice of the mold

With the mold no longer needing channels, the design differs slightly from the PDMS version, considering the fragility of the Agar Agar gel. If the tubes do not extend from the mold, as illustrated in Figure 3.8, the glass can be slid out of the slit, facilitating easy removal of the gel. Alternatively, if the tubes project from the mold, the design in Figure 3.9 is more suitable. Here, the mold is disassembled along the direction of the tubes, allowing for straightforward removal of the gel from the middle part of the mold.

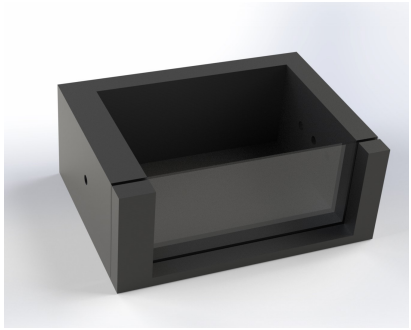

Figure 3.8: Mold with a removal glass for Agar Agar

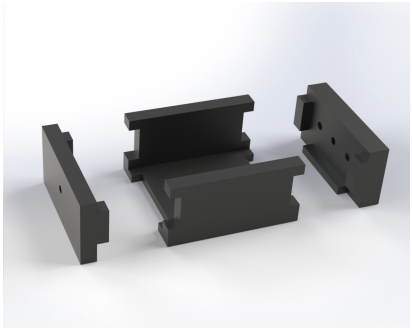

Figure 3.9: Interlocking mold for Agar Agar

3.2 Real-time Image Acquisition

To obtain images with the ultrasound (US) machine, it's necessary to apply US gel[3] to ensure a medium that facilitates US wave transmission between the probe and the Agar Agar gel, replacing air. For real-time imaging using the US Imaging machine[4], various options were explored. Initially, attempting to connect the computer to the machine via an Ethernet cable for high throughput was unsuccessful, despite successful pinging between devices. Upon contacting the company regarding this issue, it was revealed that the machine's functionalities were limited by its age. Consequently, an alternative approach using an HDMI cable was pursued. However, since the computer only has an output port, a HDMI to USB converter[5] was utilized, allowing the USB port to function as the input, akin to standard cameras. Although the converter can provide full HD video at 60 fps, the resulting characteristics are outlined in Table 3.1. The low frame rate comes from the machine itself because when connected to a screen with HDMI, it is 10 fps as well.

fps	**Resolution**	**Latency**
10	Full HD	0.1s

Table 3.1: Characteristics of the real-time imaging through HDMI

[3]Smooth Glide from Celeste
[4]Sonoscape E2
[5]Elgato Cam Link 4K

3.3 Pumps

To regulate the flow rate within the channels and automate the injection of MBs, the best approach is to use a syringe pump[6]. However, in cases with multiple outputs, without a pump to draw in the MBs, the flow rate in each output channel may differ. Therefore, an output pump addresses this issue and allows for the reuse of MBs. By employing a single pump for the output channels, equipped with the syringe holder illustrated in Figure 3.10, several syringes can be attached, ensuring a uniform flow rate.

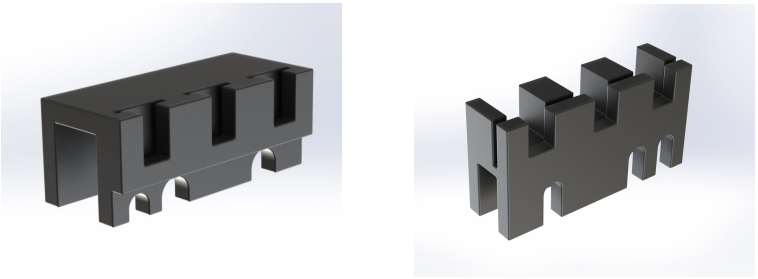

Figure 3.10: Syringe holder parts

3.4 Final Setup

Once everything is set up, the arrangement resembles Figure 3.11. The computer is connected to the US machine via an HDMI cable. The probe is positioned arbitrarily on one side of the Agar Agar gel. MBs[7] are injected into the channels by the syringe on the left, drawn out by the syringes on the output pump. Lastly, a transducer, powered by the function generator on the right, is positioned on one side of the gel to control the MBs.

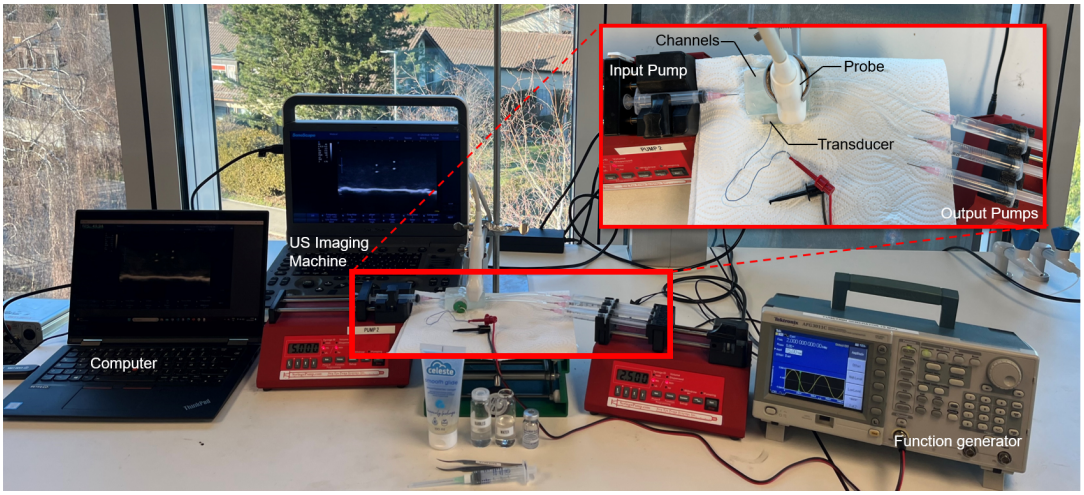

Figure 3.11: Final Setup

[6]New Era NE-1000
[7]Bracco SonoVue

Chapter 4

Tracker

4.1 Anatomical filtering

Before employing tracking algorithms, a crucial initial step involves preprocessing. The aim is to extract the Region of Interest (ROI), thereby minimizing the risk of detecting false positives (FP), by applying a mask on the channels. Two scenarios need consideration as the probe placement can vary: parallel and perpendicular cross-sections.

4.1.1 Parallel cross section

This cross-section is useful for detecting and tracking MBs while moving the probe along the channels. Since the parallel cross-section of the channels appears as circles, the objective is to identify circular patterns in the image. To aid in this task, one can leverage the information regarding the diameter size of the channels. With the image scale provided, this process can be automated.

Get Diameter of the Channels

The display of the scale on the image is always the same. Therefore, in order to detect the digits, a template matching with the numbers 1 and 2, for instance, is really efficient. Further details on this template matching process are provided in Section 4.2. Upon performing cross-correlation with the templates, the highest peak in the resulting image denotes the precise digit position. The pixel distance between digits 1 and 2 corresponds to a length of 1 cm as depicted in Figure 4.1. Given that the channel diameter is approximately 2.5 mm, dividing the distance between 1 and 2 by 4 yields the diameter size in pixels. This procedure is executed either at the onset of the tracking algorithm or whenever the scale changes

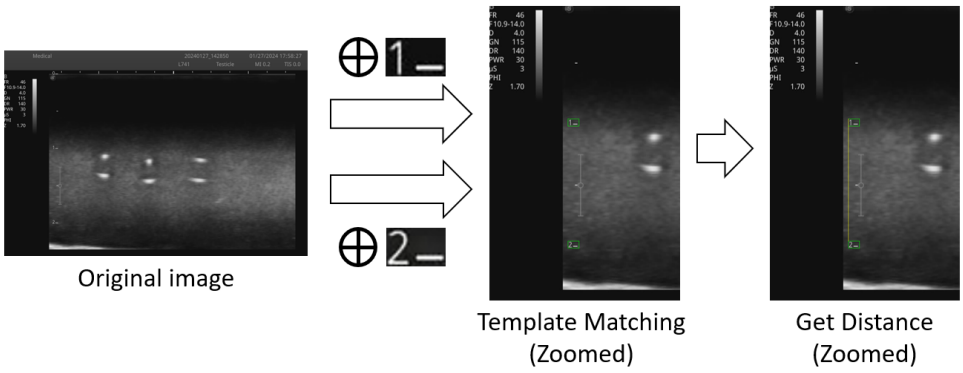

Figure 4.1: Automatic Scale Detection

Full process

Firstly, Gaussian blurring is applied to the image to achieve smoothness and remove abrupt intensity changes. Following this, a circle Hough Transform [24] is executed utilizing the `cv2.HoughCircles` function from OpenCV, where the minimum and maximum radii determined from the preceding step are automatically employed. Subsequently, the extracted circle parameters (position, radius) enable the creation and application of a mask to the original image, as illustrated in Figure 4.2.

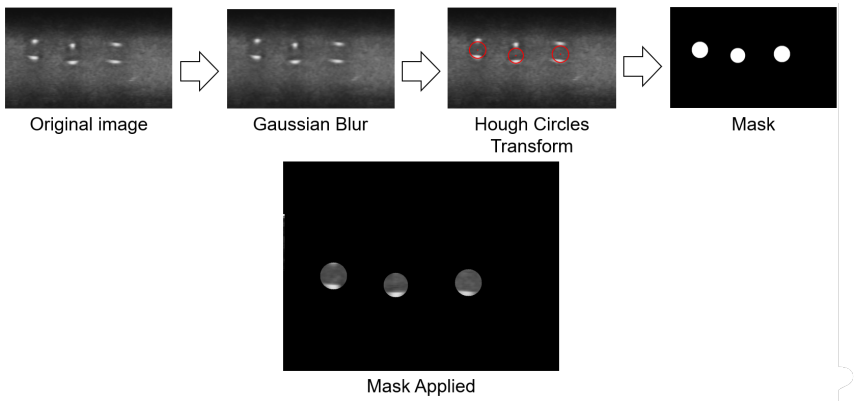

Figure 4.2: Anatomical Filtering for the parallel cross section

4.1.2 Perpendicular cross section

This cross-section is beneficial for gaining an overview of the channel network and tracking the movement of MBs without requiring probe movement.

Full process

The procedure in this case differs slightly. Since the perpendicular cross-sections are no longer circular but rather polygons of varying shapes depending on the number of bifurcations, the approach changes. Illustrated in Figure 4.3, the example depicts the process with a single-channel configuration without forks. Initially, a threshold using Otsu's method is applied. Subsequently, multiple iterations of morphological closing are performed to connect the borders of the channel. Finally, to isolate only the channel within the ROI and remove the surrounding areas, several iterations of erosion are applied.

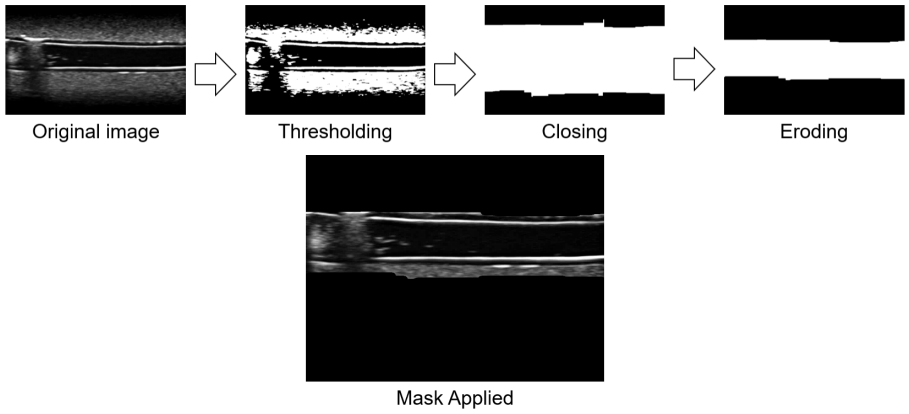

Figure 4.3: Anatomical Filtering for the perpendicular cross section

4.2 Microbubble Detection

Object detection in computer vision is a complex task that requires a good understanding of the problem in order to find the appropriate method to the problem.

4.2.1 Template Matching

In the case of the MBs in US imaging, they are only represented as a white ellipsoid, which makes them easily recognizable but hardly differentiable. The most appropriate and the most computationally efficient approach is the template matching [25]. The principle is described as following. A prechosen template that represents the object one want to detect (here a MB like represented in Figure 4.4) is cross-correlated to the image like demonstrated in Eq 4.1.

$$R(x,y) = \sum_{i=1}^{m}\sum_{j=1}^{n} I(x+i-1, y+j-1) \cdot T(i,j) \quad (4.1)$$

Figure 4.4: Template

where $R(x,y)$ represents the output of the cross-correlation operation at location (x,y), $I(x,y)$ denotes the intensity of the pixel at location (x,y) in the image, $T(i,j)$ represents the intensity of the pixel at location (i,j) in the template, and m and n are the dimensions of the template.
The peaks in the resulting image represent the locations of the object. To identify these locations, a threshold is employed to isolate all peaks above a predefined value. An illustration of the template matching process is provided in Figure 4.5, showcasing the corresponding MBs in Figure 4.6.

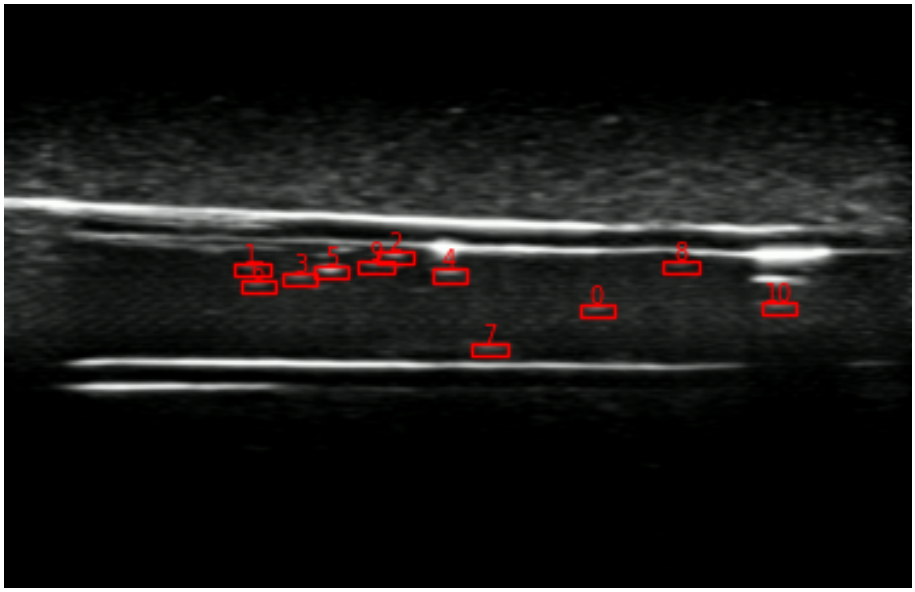

Figure 4.5: Example of Microbubbles detection with template matching

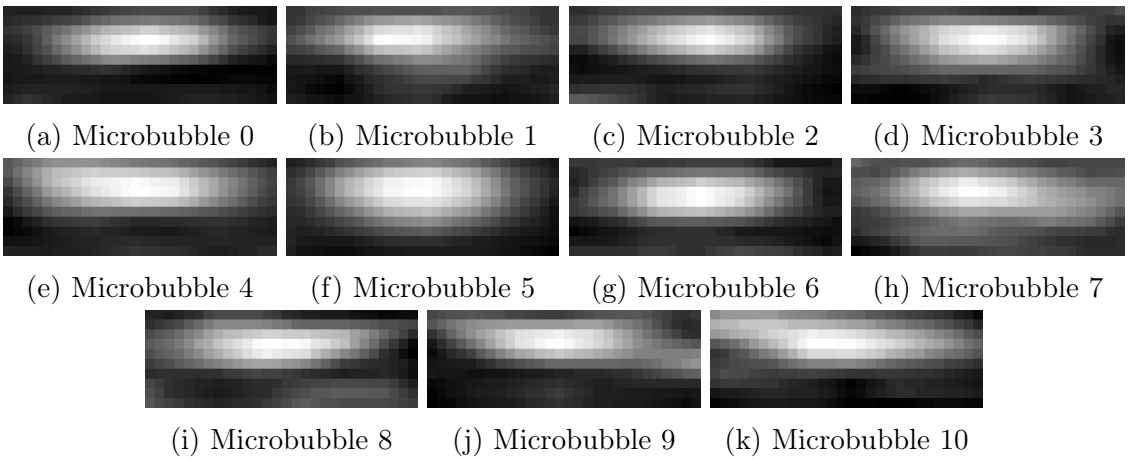

(a) Microbubble 0 (b) Microbubble 1 (c) Microbubble 2 (d) Microbubble 3

(e) Microbubble 4 (f) Microbubble 5 (g) Microbubble 6 (h) Microbubble 7

(i) Microbubble 8 (j) Microbubble 9 (k) Microbubble 10

Figure 4.6: Corresponding Microbubbles from Figure 4.5

4.2.2 Non-Maximum Suppression

A problem that arises when performing the detection is the fact that the same MB can be detected several times but with a location different of a few pixels. In order to counter this, a Non-Maximum Suppression (NMS) [26] step is necessary. It works by selecting the highest-scoring detection in a local neighborhood and suppressing all other detections that overlap significantly with it. Intersection over Union (IoU) is integrated into NMS by evaluating the degree of overlap between retained bounding boxes with the formula in Eq 4.2.

$$\text{IoU}(A, B) = \frac{\text{Area of Intersection}(A, B)}{\text{Area of Union}(A, B)} \tag{4.2}$$

where:

- A : Bounding box 1
- B : Bounding box 2
- Area of Intersection(A, B) : Area of overlap between A and B
- Area of Union(A, B) : Total area covered by A and B

As the pseudocode in Figure 4.7 explains, after applying NMS to retain only the highest-scoring detections, IoU measures the overlap between these retained boxes. If the IoU between two boxes exceeds a certain threshold, one of the detections is suppressed to ensure non-redundancy as shown in Figure 4.8 where 3 bounding boxes were displayed for the same MB. This combination of NMS and IoU guarantees that only the most relevant and non-overlapping detections are preserved, enhancing the accuracy and reliability of object detection algorithms.

Algorithm Non-Max Suppression

```
procedure NMS(B,c)
    B_nms ← ∅                                   Initialize empty set
    for b_i ∈ B do                              => Iterate over all the boxes
        discard ← False                         Take boolean variable and set it as false. This variable indicates whether b(i) should be kept or discarded
        for b_j ∈ B do                          Start another loop to compare with b(i)
            if same(b_i, b_j) > λ_nms then      If both boxes having same IOU
                if score(c, b_j) > score(c, b_i) then
                    discard ← True              Compare the scores. If score of b(i) is less than that of b(j), b(i) should be discarded, so set the flag to True.
        if not discard then                     Once b(i) is compared with all other boxes and still the discarded flag is False, then b(i) should be considered. So add it to the final list.
            B_nms ← B_nms ∪ b_i
    return B_nms                                Do the same procedure for remaining boxes and return the final list
```

Figure 4.7: NMS Algorithm

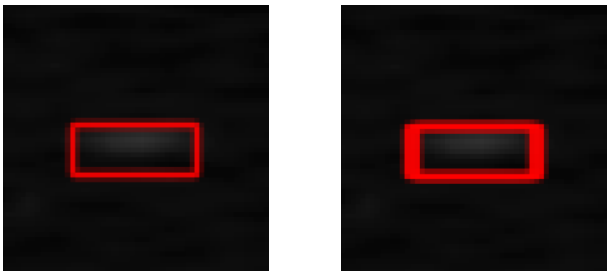

(a) With NMS (b) Without NMS

Figure 4.8: Difference between Microbubble detection with and without NMS

4.3 DeepSORT

The tracking algorithm needs to meet certain criteria: real-time capability, multiple object tracking (MOT) functionality, and resilience against occlusions. One widely used open-source tracker that fulfills these requirements is Simple Online and Realtime Tracking with a Deep Association Metric (DeepSORT) [27]. Built upon the SORT algorithm [28], DeepSORT incorporates a deep appearance descriptor [29]. It employs significant concepts that need closer examination.

4.3.1 Kalman Filter

The Kalman filter [30], manages a state comprising eight variables: (u,v,a,h,u',v',a',h'), representing bounding box centers, aspect ratio, and image height along with their respective velocities. Assumed with a linear velocity model, the filter mitigates detection noise and utilizes prior state to predict bounding box fits. Each detection generates a "Track" with comprehensive state information, facilitating track management, including the removal of long-inactive tracks and preventing duplicate tracks by imposing a minimum detection threshold during initial frames.

4.3.2 Assignment Problem

In DeepSORT, the assignment problem involves associating existing tracks with incoming detections, a task vital for maintaining accurate object tracking. To tackle this challenge, the Hungarian algorithm [31] is employed. This algorithm optimally matches tracks to detections by minimizing the total assignment cost, typically calculated using distance metrics such as the Mahalanobis distance. By considering the distribution-based nature of the data and accounting for uncertainties from the Kalman filter, the Mahalanobis distance facilitates accurate association between tracks and detections. Together, the Hungarian algorithm and the Mahalanobis distance form a robust framework for solving the assignment problem in DeepSORT, ensuring reliable object tracking in complex scenarios.

4.3.3 Training

Initially, DeepSORT was trained on the MARS dataset [32], which primarily features people. Adapting the tracker to MBs requires a dataset comprising ultrasound images of MBs. Unfortunately, no publicly available dataset of this nature exists, and limited time and data hindered the creation of a custom dataset. Consequently, DeepSORT is utilized with the original MARS dataset.

4.4 Pipeline

Once all components are interconnected, the completed pipeline looks like the configuration depicted in Figure 4.9, generating a video output showcased in Figure 4.10. Initially, an anatomical filtering step is executed to identify the channels. Subsequently, the tracker incorporates MB detection via template matching and utilizes DeepSORT to provide the bounding box positions.

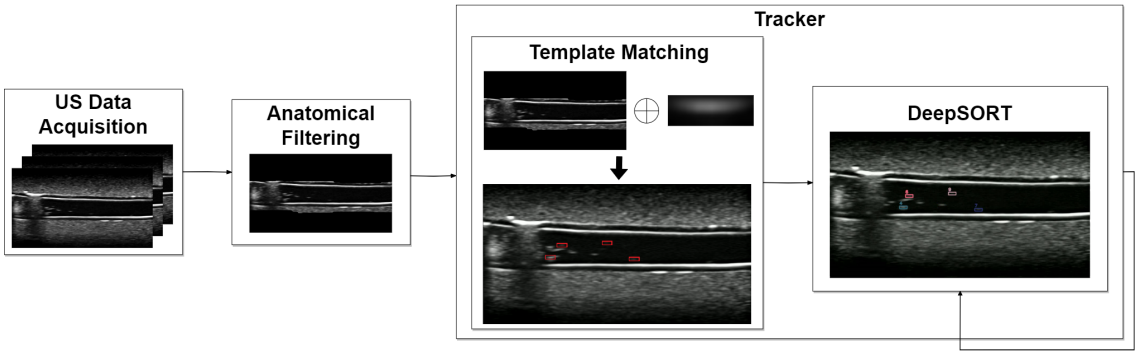

Figure 4.9: Tracking Pipeline

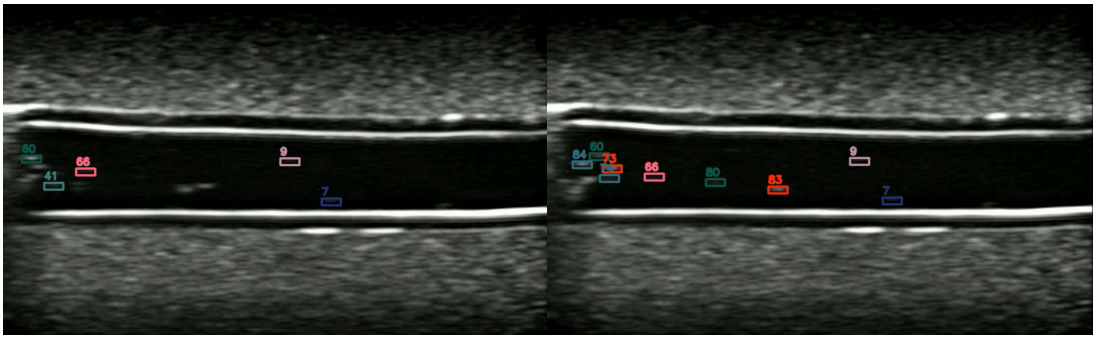

(a) Tracker at time t

(b) Tracker at time $t + 1s$

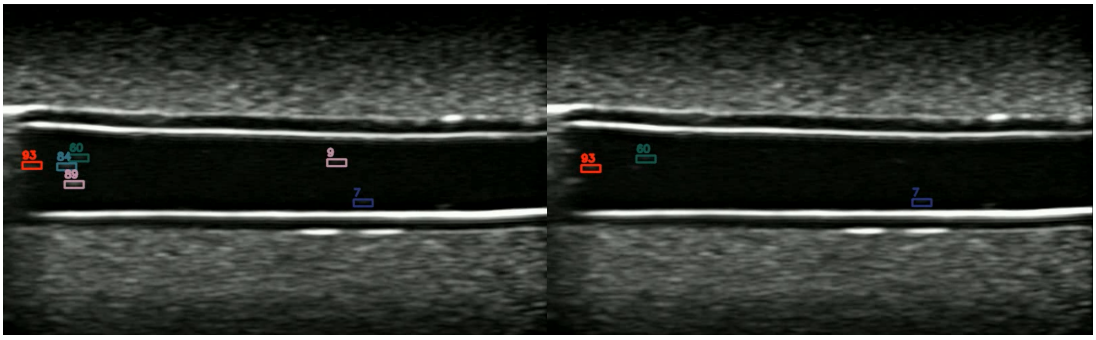

(c) Tracker at time $t + 2s$

(d) Tracker at time $t + 3s$

Figure 4.10: Tracker over 3 seconds

Chapter 5

Results and Discussion

5.1 Control of Microbubbles

While working on the tracker, I started to control the MBs in order to use the tracker as a feedback system. However, I realized that controlling MBs is more complicated than expected, firstly due to the effect of the US probe on the MBs described in section 1.1.2 and due to the different acoustic effects of the different transducers on the channels. After trying without success different types of transducer with a low flow rate (<1.5 mL/min), I started to test flow rates above 2mL/min. After testing with all the different transducers (resonance frequency of 1 MHz, 2 MHz...etc), I only obtained results with a MB concentration of 40μL/100mL using a HIFU of a resonance frequency of 2 MHz on the fork with 2 channels.

Before presenting the results, let us define the left and right channel as shown in Figure 5.1 in order to be clear in the next parts.

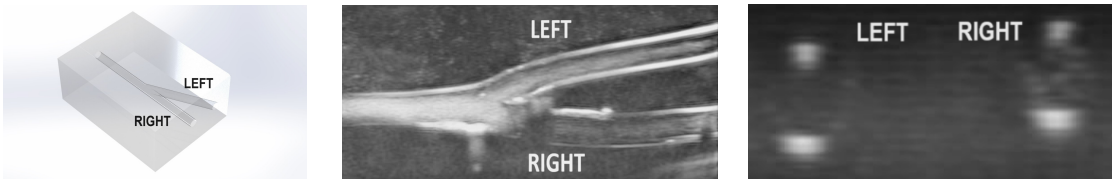

Figure 5.1: Annotation of the left and right channel

5.1.1 Direct Microbubbles to the left channel

The Figures 5.2 and 5.3 show visually what is happening to the MBs under a flow rate of 5mL/min when the HIFU is triggered. In the perpendicular cross section, the trigger has the most effect with 7V and in the parallel cross section it is 15V. As described in section 1.1.2, this difference is due to the fact that the probe has a big effect when the MBs are observed through the perpendicular cross section because it sees the MBs for a long time (contrary to the parallel cross section where the MBs are seen for a brief instant).

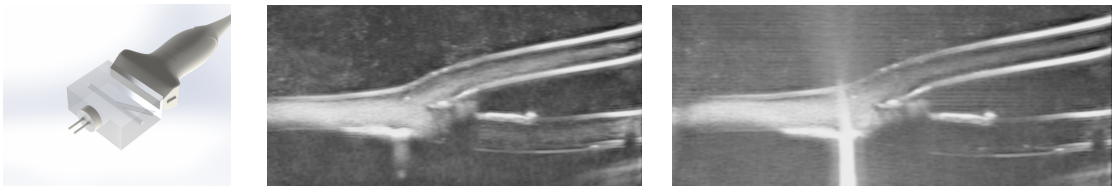

(a) Position of the probe (b) Before Trigger (c) After Trigger

Figure 5.2: Microbubbles directed to the left channel observed through the perpendicular cross section of the channels

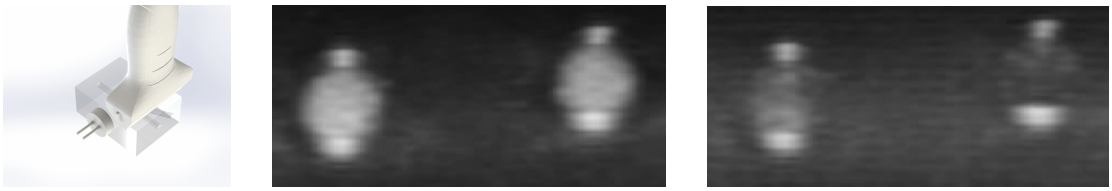

(a) Position of the probe (b) Before Trigger (c) After Trigger

Figure 5.3: Microbubbles directed to the left channel observed through the parallel cross section of the channels

The Figure 5.4 shows numerically the results. It is a graph of the average intensity in the left and right channel calculated in the parallel cross section of the channels as MBs are displayed as white pixels. At each time step, the average intensity of the cross section is normalized by the average of the average intensity before the trigger as described in Eq 5.1. The graph shows that before the trigger, both channels are more or less stable around the same value. However, from 1 second after the trigger, a gap between the left and right channel is created of up to 20%.

$$[h!]AI(t) = \frac{\sum_S \frac{I(x,y,t)}{N}}{\sum_{\tau=t_0}^{t_{\text{trigger}}} \sum_S \frac{I(x,y,\tau)}{N(t_{\text{trigger}}-t_0)}} \quad , (x,y) \in S, t \in [t_0; \infty[, \tau \in [t_0; t_{\text{trigger}}] \quad (5.1)$$

Where:

- $AI(t)$ is the average intensity of the cross section at time t.
- S is the set of pixels representing the parallel cross section of the left or right channel.
- N is the number of pixels in S.
- $I(x, y, t)$ is the intensity of the pixel at the position (x,y) and at time t.
- t_0 is the initial time.
- t_{trigger} is the time when there is the trigger.

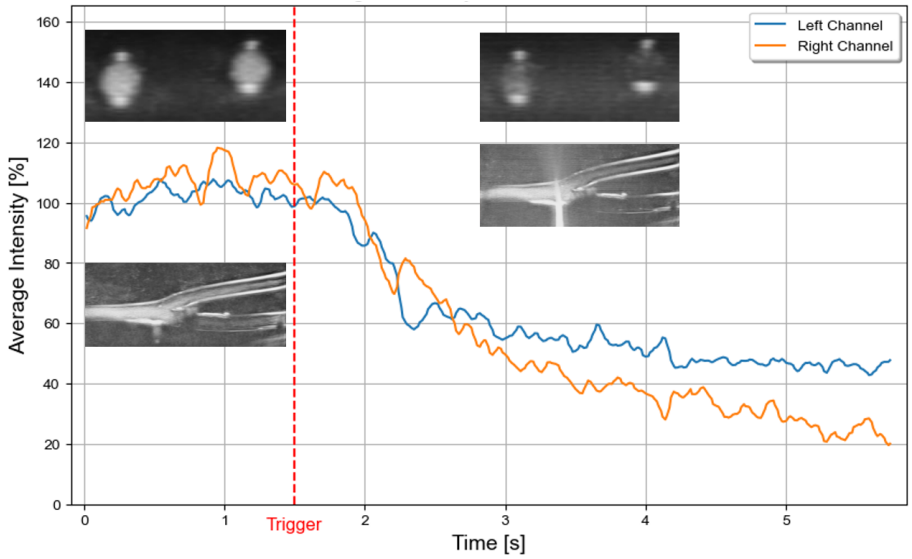

Figure 5.4: Average Intensity in the two channels

5.1.2 Direct Microbubbles to the right channel

The Figures 5.5 and 5.6 show visually what is happening to the MBs under a flow rate of 5mL/min when the HIFU is triggered. As in section 5.1.1, in the perpendicular cross section, the trigger has the most effect with 7V and in the parallel cross section it is 15V, and this is due to the same reasons.

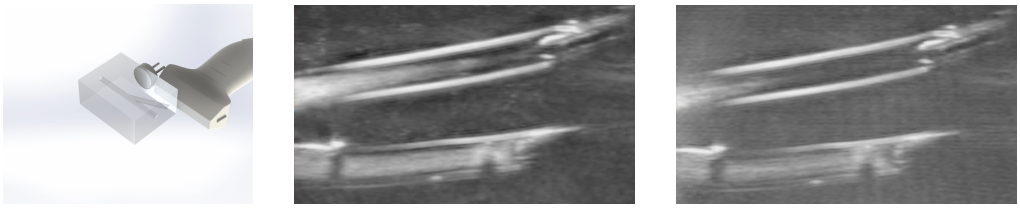

(a) Position of the probe (b) Before Trigger (c) After Trigger

Figure 5.5: Microbubbles directed to the right channel observed through the perpendicular cross section of the channels

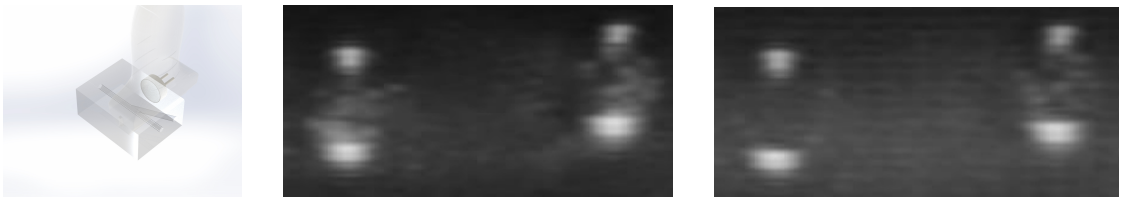

(a) Position of the probe (b) Before Trigger (c) After Trigger

Figure 5.6: Microbubbles directed to the right channel observed through the parallel cross section of the channels

The Figure 5.7 shows numerically the results. It is also a graph of the average intensity in the left and right channel calculated in the parallel cross section of the channels as the Eq 5.1 describes. The graph shows that before the trigger, both channels are more or less stable around the same value. However, from a few tenths of seconds after the trigger, a big gap between the left and right channel is created of up to 140%.

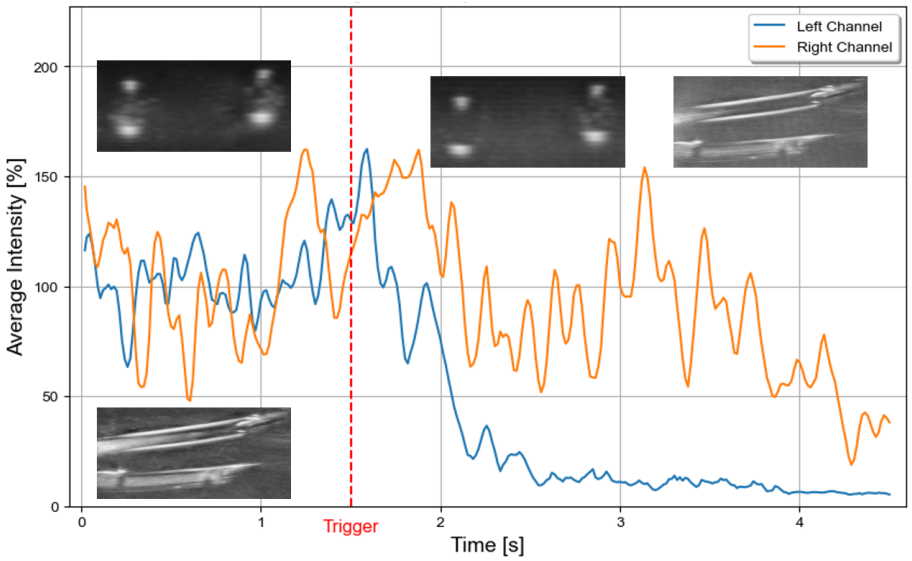

Figure 5.7: Average Intensity in the two channels

5.2 Tracker

Given that the tracker comprises both detection and tracking components, its performance evaluation can be categorized accordingly. It's worth noting, as discussed in section 5.1, that controlling the MBs presents unexpected challenges, affecting the flow rate and thus impacting the tracker's functionality as individual MBs become indistinguishable. Therefore, the performance metrics are only derived from the video depicted in Figure 4.10 which is simply MBs at a flowrate of 2,2mL/min through a commercial TMMP[1].

5.2.1 Detection

Precision

Precision measures the accuracy of positive predictions made by the model. It calculates the ratio of true positive predictions to the total number of positive predictions made, indicating the proportion of correctly identified positive instances among all instances predicted as positive. Mathematically, precision is defined as:

$$\text{Precision} = \frac{\text{True Positives}}{\text{True Positives} + \text{False Positives}}$$

[1] from CIRS

Recall

Recall, also known as sensitivity or true positive rate, measures the model's ability to capture all positive instances. It calculates the ratio of true positive predictions to the total number of actual positive instances in the data set, indicating the proportion of correctly identified positive instances among all actual positive instances. Mathematically, recall is defined as:

$$\text{Recall} = \frac{\text{True Positives}}{\text{True Positives} + \text{False Negatives}}$$

F1 Score

The F1 score is the harmonic mean of precision and recall, providing a single metric that balances both precision and recall. It is useful for evaluating the overall performance of a model, especially when there is an imbalance between the number of positive and negative instances. Mathematically, the F1 score is defined as:

$$\text{F1 Score} = 2 \times \frac{\text{Precision} \times \text{Recall}}{\text{Precision} + \text{Recall}}$$

Results

Based on the obtained results, it is evident that employing the anatomical filter significantly enhances the precision, with a notable increase from 0.58 to 0.97, thereby reducing the number of false positives detected outside of the channel as illustrated in Figure 5.8. However, despite this improvement, the recall remains constant at 0.43, indicating that the anatomical filter does not effectively address the issue of missed detections, possibly due to the nature of template matching used for MB detection. Consequently, the F1 score sees a modest increase from 0.49 to 0.59 with the application of the anatomical filter, reflecting the improved balance between precision and recall. It is essential to note that the relatively low recall may be attributed to the inherent limitations of template matching for MB detection, which could miss certain instances, particularly in regions with complex anatomical structures.

	Precision	**Recall**	**F1 Score**
With filter	0.97	0.43	0.59
Without filter	0.58	0.43	0.49

Table 5.1: Detection Performance Metrics with and without anatomical filter

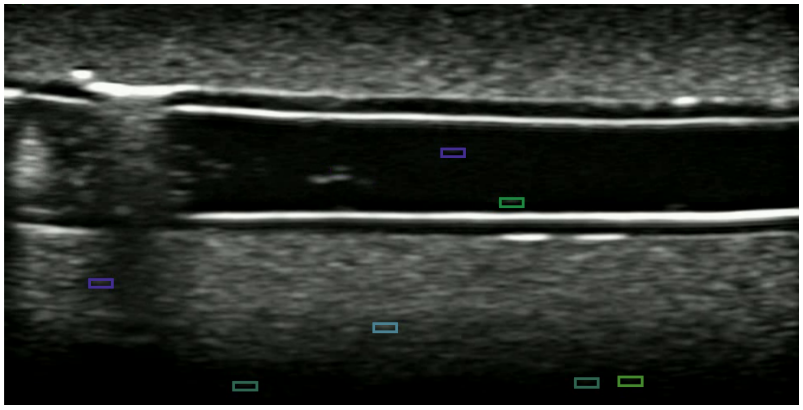

Figure 5.8: Detection of Microbubbles without the anatomical filter

5.2.2 Tracking

Multiple Object Tracking Accuracy (MOTA)

Multiple Object Tracking Accuracy (MOTA) is a metric used to evaluate the overall performance of a tracking system. It considers both false positives, false negatives, and identity switches, providing a comprehensive measure of tracking accuracy. The MOTA score ranges from 0 to 1, where higher values indicate better tracking accuracy. The formula for MOTA is as follows:

$$\text{MOTA} = 1 - \frac{\text{FN} + \text{FP} + \text{IDsw}}{\text{GT}}$$

Where:

- FN: Number of false negatives (missed detections).
- FP: Number of false positives (incorrect detections).
- IDsw: Number of identity switches.
- GT: Total number of ground truth objects.

IDF1 Score

IDF1 (Identification F1) score is a metric used to evaluate the tracking accuracy in multiple object tracking scenarios. It considers the harmonic mean of precision and recall for correctly identified objects. The formula for IDF1 score is given by:

$$\text{IDF1} = \frac{2 \times \text{TP}}{2 \times \text{TP} + \text{FP} + \text{FN}}$$

Where:

- TP: True positives (correctly identified objects).
- FP: False positives (incorrectly identified objects).
- FN: False negatives (missed identifications).

Results

The tracking performance, as measured by the MOTA score, is found to be 0.42, indicating that there is room for improvement in optimizing the tracking algorithm. Additionally, the IDF1 score, which considers both identification and localization accuracy, stands at 0.59. However, it's important to note that the tracking system is not yet fully optimized, as discussed in Section 5.1. Further refinement and optimization of the tracking algorithm are essential to enhance the accuracy and reliability of MB tracking.

	MOTA	**IDF1**
DeepSORT	0.42	0.59

Table 5.2: Tracking Performance

Chapter 6

Conclusion and Outlook

This thesis proposes a novel method for creating channels using Heat Shrink Tubes and Agar Agar to facilitate the visualization of MBs with US imaging.
Furthermore, a real-time feedback solution has been established using the HDMI cable. Despite achieving a maximum performance of only 10 Hz, Full HD resolution, and a 0.1-second latency, this setup is sufficient for an accurate feedback system.
A fresh method for MB tracking using US imaging has been investigated, incorporating the DeepSORT algorithm trained on the MARS dataset. MB detection is achieved through template matching, preceded by anatomical filtering that applies to both the parallel and perpendicular cross-sections of the channels.
Finally, a viable method of guiding MB trajectories has been uncovered under high flow rates, such as 5 mL/min. By utilizing a HIFU transducer in a bifurcation with two channels, the MBs can be steered in a predetermined direction. However, due to the intense flow rate and the high MB density in the water, it becomes unfeasible to detect and track them using the tracker outlined in section 4.

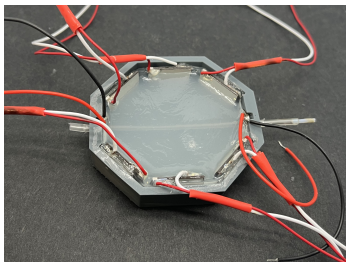

Figure 6.1: Octagon of 2 MHz transducers with a single channel

While the achieved results present promise, there are areas for further enhancement in both the tracker and control system of the MBs. Firstly, refining the experimental setup is imperative. Given the limitations of Agar Agar, particularly its fragility and the presence of air bubbles within the matrix, enhancing the robustness of the Phantom skin by eliminating these bubbles and by making it more solid could significantly improve performance. Exploring methods to influence MBs within the fork using three channels represents a promising avenue for future research, with the potential to expand to more intricate channel designs. Additionally, while the design of the transducer octagon depicted in Figure 6.1 proved ineffective, exploring its application with HIFU presents a promising alternative. Lastly, given the occasional success of alternative transducers, investigating their compatibility with both high and low flow rates could yield valuable insights. Moreover, if feasible to influence individual MBs while tracking them, customizing the tracker through training on MBs data could lead to substantial improvements in performance.

Appendix A

Tuning parameters

Parameter	Rationale for choice	Value
n_{gauss}	↑ More extensive blurring effect ↓ Stronger, more localized blurring effect	9x9
dp	↑ Less precise circle detection ↓ Detection of finer details	1
minDist	Minimum distance between the centers of the detected circles	100
param1	↑ Make edge detection more strict ↓ More circles detection	110
param2	↑ Circle detection more stringent ↓ More circles detection	10
minRadius	Sets the lower bound for the radius of the circles	$r_{channel} - 5$
maxRadius	Sets the upper bound for the radius of the circles	$r_{channel} + 5$

Table A.1: Parameters for the Circle Hough Transform

Step	Parameter	Rationale for choice	Value
Closing	$n_{iteration}$	Number of time the closing is applied	15
	n_{kernel}	Dimension of the kernel used for closing	9x9
Eroding	$n_{iteration}$	Number of time the eroding is applied	4
	n_{kernel}	Dimension of the kernel used for eroding	40x40

Table A.2: Parameters for the anatomical filtering for the perpendicular cross section

Step	Parameter	Rationale for choice	Value
Template matching	Threshold	↑ Filter out low-confidence detections ↓ Retain lower-confidence detections	0.92
NMS	score_threshold	↑ Keep high-confidence bounding boxes ↓ Retain more boxes with lower scores	0.92
	nms_threshold	↑ More aggressive suppression ↓ More overlapping boxes	0.5

Table A.3: Parameters for the microbubble detection

Bibliography

[1] Adem Ozcelik, Ryan Becker, and Tony Jun Huang. *Acoustic Technologies in Biology and Medicine*. Wiley, 2023.

[2] LE Derchi, G Rizzatto, and L Solbiati. Color-doppler instruments: their design principles and modes of use. *La Radiologia Medica*, 84(5):523–531, 1992.

[3] Julia H Miao. The art and science of ultrasound imaging: medical applications of ultrasound in diagnosis and therapy and its impact on patient care. *Cardiovascular Diagnosis and Therapy*, 13(1):109, 2023.

[4] Fatiha M. Benslimane, Maha Alser, Zain Z. Zakaria, Anju Sharma, Hana A. Abdelrahman, and Huseyin C. Yalcin. Adaptation of a mice doppler echocardiography platform to measure cardiac flow velocities for embryonic chicken and adult zebrafish. *Frontiers in Bioengineering and Biotechnology*, 7, 2019. ISSN 2296-4185. doi: 10.3389/fbioe.2019.00096. URL `https://www.frontiersin.org/articles/10.3389/fbioe.2019.00096`.

[5] Robert W. Gill. Measurement of blood flow by ultrasound: Accuracy and sources of error. *Ultrasound in Medicine & Biology*, 11(4):625–641, 1985. ISSN 0301-5629. doi: https://doi.org/10.1016/0301-5629(85)90035-3. URL `https://www.sciencedirect.com/science/article/pii/0301562985900353`.

[6] Outi Supponen, Awaneesh Upadhyay, Jordan Lum, Francesco Guidi, Todd Murray, Hendrik J Vos, Piero Tortoli, and Mark Borden. The effect of size range on ultrasound-induced translations in microbubble populations. *The Journal of the Acoustical Society of America*, 147(5):3236–3247, 2020.

[7] Dana Middleton Kerr and William Dana Middleton. Reflections on the ultrasound mirror image artifact. *Ultrasound Quarterly*, 36(4):287–299, 2020.

[8] Richard J Browning and Eleanor Stride. Microbubble-mediated delivery for cancer therapy. *Fluids*, 3(4):74, 2018.

[9] Ching-Hsiang Fan and Chih-Kuang Yeh. Microbubble-enhanced focused ultrasound-induced blood–brain barrier opening for local and transient drug delivery in central nervous system disease. *Journal of Medical Ultrasound*, 22(4):183–193, 2014. ISSN 0929-6441. doi: https://doi.org/10.1016/j.jmu.2014.11.001. URL `https://www.sciencedirect.com/science/article/pii/S0929644114001635`.

[10] Silke Roovers, Tim Segers, Guillaume Lajoinie, Joke Deprez, Michel Versluis, Stefaan C. De Smedt, and Ine Lentacker. The role of ultrasound-driven microbubble dynamics in drug delivery: From microbubble fundamentals to clinical translation. *Langmuir*, 35(31):10173–10191, 2019. doi: 10.1021/acs.langmuir.8b03779. URL https://doi.org/10.1021/acs.langmuir.8b03779. PMID: 30653325.

[11] Alexia Del Campo Fonseca, Tobias Kohler, and Daniel Ahmed. Ultrasound-controlled swarmbots under physiological flow conditions. *Advanced Materials Interfaces*, 9(26):2200877, 2022. doi: https://doi.org/10.1002/admi.202200877. URL https://onlinelibrary.wiley.com/doi/abs/10.1002/admi.202200877.

[12] Matthijs Schrage, Mahmoud Medany, and Daniel Ahmed. Ultrasound microrobots with reinforcement learning. *Advanced Materials Technologies*, 8(10), March 2023. ISSN 2365-709X. doi: 10.1002/admt.202201702. URL http://dx.doi.org/10.1002/admt.202201702.

[13] Qianqian Wang and Li Zhang. External power-driven microrobotic swarm: From fundamental understanding to imaging-guided delivery. *ACS Nano*, 15 (1):149–174, 2021. doi: 10.1021/acsnano.0c07753. URL https://doi.org/10.1021/acsnano.0c07753. PMID: 33417764.

[14] Sofie Bech Andersen, Iman Taghavi, Hans Martin Kjer, Stinne Byrholdt Søgaard, Carsten Gundlach, Vedrana Andersen Dahl, Michael Bachmann Nielsen, Anders Bjorholm Dahl, Jørgen Arendt Jensen, and Charlotte Mehlin Sørensen. Evaluation of 2d super-resolution ultrasound imaging of the rat renal vasculature using ex vivo micro-computed tomography. *Scientific reports*, 11 (1):24335, 2021.

[15] Chengwu Huang, Matthew R Lowerison, Joshua D Trzasko, Armando Manduca, Yoram Bresler, Shanshan Tang, Ping Gong, U-Wai Lok, Pengfei Song, and Shigao Chen. Short acquisition time super-resolution ultrasound microvessel imaging via microbubble separation. *Scientific reports*, 10(1):6007, 2020.

[16] Kristoffer B. Hansen, Carlos A. Villagómez-Hoyos, Jens Christian Brasen, Konstantinos Diamantis, Vassilis Sboros, Charlotte Mehlin Sørensen, and Jørgen Arendt Jensen. Robust microbubble tracking for super resolution imaging in ultrasound. In *2016 IEEE International Ultrasonics Symposium (IUS)*, pages 1–4, 2016. doi: 10.1109/ULTSYM.2016.7728793.

[17] Xingzhou Du, Qianqian Wang, Dongdong Jin, Philip Wai Yan Chiu, Chi Pui Pang, Kelvin Kam Lung Chong, and Li Zhang. Real-time navigation of an untethered miniature robot using mobile ultrasound imaging and magnetic actuation systems. *IEEE Robotics and Automation Letters*, 7(3):7668–7675, 2022. doi: 10.1109/LRA.2022.3184445.

[18] Qianqian Wang, Shihao Yang, and Li Zhang. Magnetic actuation of a dynamically reconfigurable microswarm for enhanced ultrasound imaging contrast. *IEEE/ASME Transactions on Mechatronics*, 27(6):4235–4245, 2022. doi: 10.1109/TMECH.2022.3151983.

[19] Karim Botros, Mohammad Alkhatib, David Folio, and Antoine Ferreira. Fully automatic and real-time microrobot detection and tracking based on ultrasound imaging using deep learning. In *2022 International Conference on Robotics and Automation (ICRA)*, pages 9763–9768, 2022. doi: 10.1109/ICRA46639.2022.9812114.

[20] Giovanni Faoro, Veronica Iacovacci, and Arianna Menciassi. Optical flow and acoustic phase analysis comparison in ultrasound-based microrobot tracking. *IEEE Robotics and Automation Letters*, 9(2):1985–1992, 2024. doi: 10.1109/LRA.2024.3349815.

[21] Dimitri Ackermann and Georg Schmitz. Detection and tracking of multiple microbubbles in ultrasound b-mode images. *IEEE Transactions on Ultrasonics, Ferroelectrics, and Frequency Control*, 63(1):72–82, 2016. doi: 10.1109/TUFFC.2015.2500266.

[22] Cinzia Avigo, Nicole Di Lascio, Paolo Armanetti, Claudia Kusmic, Lucia Cavigli, Fulvio Ratto, Sandro Meucci, Cecilia Masciullo, Marco Cecchini, Roberto Pini, Francesco Faita, and Luca Menichetti. Organosilicon phantom for photoacoustic imaging. *Journal of biomedical optics*, 20:46008, 04 2015. doi: 10.1117/1.JBO.20.4.046008.

[23] Matthew Earle, Giuliano De Portu, and Elizabeth DeVos. Agar ultrasound phantoms for low-cost training without refrigeration. *African Journal of Emergency Medicine*, 6(1):18–23, 2016. ISSN 2211-419X. doi: https://doi.org/10.1016/j.afjem.2015.09.003. URL `https://www.sciencedirect.com/science/article/pii/S2211419X15001111`.

[24] Mohamed Rizon, Haniza Yazid, Puteh Saad, ali yeon md shakaff, and Abdul Saad. Object detection using circular hough transform. *American Journal of Applied Sciences*, 2, 12 2005. doi: 10.3844/ajassp.2005.1606.1609.

[25] Roberto Brunelli. Template matching techniques in computer vision. 09 2008.

[26] A. Neubeck and L. Van Gool. Efficient non-maximum suppression. In *18th International Conference on Pattern Recognition (ICPR'06)*, volume 3, pages 850–855, 2006. doi: 10.1109/ICPR.2006.479.

[27] Nicolai Wojke, Alex Bewley, and Dietrich Paulus. Simple online and realtime tracking with a deep association metric. In *2017 IEEE international conference on image processing (ICIP)*, pages 3645–3649. IEEE, 2017.

[28] Alex Bewley, Zongyuan Ge, Lionel Ott, Fabio Ramos, and Ben Upcroft. Simple online and realtime tracking. In *2016 IEEE International Conference on Image Processing (ICIP)*, pages 3464–3468, 2016. doi: 10.1109/ICIP.2016.7533003.

[29] Nicolai Wojke and Alex Bewley. Deep cosine metric learning for person re-identification. In *2018 IEEE Winter Conference on Applications of Computer Vision (WACV)*, pages 748–756. IEEE, 2018. doi: 10.1109/WACV.2018.00087.

[30] R. E. Kalman. A New Approach to Linear Filtering and Prediction Problems. *Journal of Basic Engineering*, 82(1):35–45, 03 1960. ISSN 0021-9223. doi: 10.1115/1.3662552. URL `https://doi.org/10.1115/1.3662552`.

[31] H. W. Kuhn. The hungarian method for the assignment problem. *Naval Research Logistics Quarterly*, 2(1-2):83–97, 1955. doi: https://doi.org/10.1002/nav.3800020109. URL `https://onlinelibrary.wiley.com/doi/abs/10.1002/nav.3800020109`.

[32] *MARS: A Video Benchmark for Large-Scale Person Re-identification*, 2016. Springer.

ETH
Eidgenössische Technische Hochschule Zürich
Swiss Federal Institute of Technology Zurich

Acoustic Robotics Systems Lab
Prof. Dr. D. Ahmed

Title of work:

Real-Time Ultrasound Imaging Feedback

Thesis type and date:

Semester Thesis, January 2024

Supervision:

Mahmoud Medany

Student:

Name: Lilian Laporte
E-mail: llaporte@student.ethz.ch
Legi-Nr.: 19-816-156
Semester: 5

Statement regarding plagiarism:

By signing this statement, I affirm that I have read and signed the Declaration of Originality, independently produced this paper, and adhered to the general practice of source citation in this subject-area.

Declaration of Originality:

`http://www.ethz.ch/faculty/exams/plagiarism/confirmation_en.pdf`

Zurich, 18. 2. 2024: 

Intellectual Property Agreement

The student acted under the supervision of Prof. Ahmed and contributed to research of his group. Research results of students outside the scope of an employment contract with ETH Zurich belong to the students themselves. The results of the student within the present thesis shall be exploited by ETH Zurich, possibly together with results of other contributors in the same field. To facilitate and to enable a common exploitation of all combined research results, the student hereby assigns his rights to the research results to ETH Zurich. In exchange, the student shall be treated like an employee of ETH Zurich with respect to any income generated due to the research results.
This agreement regulates the rights to the created research results.

1. Intellectual Property Rights

1. The student assigns his/her rights to the research results, including inventions and works protected by copyright, but not including his moral rights ("Urheberpersönlichkeitsrechte"), to ETH Zurich. Herewith, he cedes, in particular, all rights for commercial exploitations of research results to ETH Zurich. He is doing this voluntarily and with full awareness, in order to facilitate the commercial exploitation of the created Research Results. The student's moral rights ("Urheberpersönlichkeitsrechte") shall not be affected by this assignment.

2. In exchange, the student will be compensated by ETH Zurich in the case of income through the commercial exploitation of research results. Compensation will be made as if the student was an employee of ETH Zurich and according to the guidelines "Richtlinien für die wirtschaftliche Verwertung von Forschungsergebnissen der ETH Zürich".

3. The student agrees to keep all research results confidential. This obligation to confidentiality shall persist until he or she is informed by ETH Zurich that the intellectual property rights to the research results have been protected through patent applications or other adequate measures or that no protection is sought, but not longer than 12 months after the collaborator has signed this agreement.

4. If a patent application is filed for an invention based on the research results, the student will duly provide all necessary signatures. He/she also agrees to be available whenever his aid is necessary in the course of the patent application process, e.g. to respond to questions of patent examiners or the like.

2. Settlement of Disagreements

Should disagreements arise out between the parties, the parties will make an effort to settle them between them in good faith. In case of failure of these agreements, Swiss Law shall be applied and the Courts of Zurich shall have exclusive jurisdiction.

Zürich, 18/02/2024
Place and date


Signature